2019 International Conference on Indoor Positioning and Indoor Navigation (IPIN), 30 Sept. - 3 Oct. 2019, Pisa, Italy

EKF-based and Geometry-based Positioning under Location Uncertainty of Access Nodes in Indoor Environment

Yi Lu, Mike Koivisto, Jukka Talvitie, Mikko Valkama, and Elena Simona Lohan
Electrical Engineering, *Tampere University*, *Tampere, Finland*
{yi.lu, mike.koivisto, jukka.talvitie, mikko.valkama, elena-simona.lohan}@tuni.fi

***Abstract*—High accuracy positioning enabled by 5G cellular networks will play a crucial role in the robot-based industrial applications, where the vertical accuracy will be as significant as the 3D accuracy. Aiming at target applications relying on flying robots in industrial environments, this paper presents and formulates two positioning algorithms when the location uncertainty of the access nodes (ANs) is taken into consideration. The first algorithm is a low-complexity geometry-based 3D positioning algorithm that utilizes both time-of-arrival and angle-of-arrival measurements. The second algorithm relies on extended Kalman Filter (EKF)-based positioning, by mapping the ANs' location uncertainty into the measurement noise statistics. The performance of the two proposed method is studied in terms of 3D and vertical positioning accuracy, sensitivity to location uncertainty of the ANs, and computational complexity in indoor scenarios. Based on the conducted complexity analysis, the proposed geometry-based algorithm is computationally more efficient than the EKF-based algorithm. In addition, the proposed geometry-based positioning method demonstrates a higher robustness against a high location uncertainty of ANs than the considered EKF-based method.**

***Index Terms*—robot tracking, 5G networks, indoor positioning, non-linear mapping, location uncertainty of access nodes**

I. Introduction

Several applications of the future Industrial Internet of Things (IIoT) systems empowered by 5G networks are likely to require a flying robot to perform various tasks, such as air quality monitoring, between-floor transportation of goods, worker safety control, problem diagnosis or remote maintenance for high-elevation spaces, which are difficult to access manually. The 3D positioning plays an important role in the use cases where the flying robots must be localized and tracked continuously and reliably, both in the horizontal plane and in the vertical plane [1]. Accurate methods for robot positioning typically rely on location-dependent radio measurements, such as the received signal strength, delay and/or angle measurements coming from access nodes (ANs) with precisely known locations [2]–[7]. However, in the case of mobile or wheel-mounted ANs or industrial environments with assets regularly displaced or moved around, the knowledge of the locations of the ANs might not be precise. In other words, depending on device-centric positioning or network-centric positioning, the location-dependent radio measurements are thought to be transmitted from or received at a location that is not the actual location of the ANs. A classical solution to the problem is to perform the joint estimation of locations of both ANs and robot using Bayesian filters, e.g., the extended Kalman filter (EKF). However, an extremely large state vector due to the joint estimation leads to an increased computational complexity that may be unfeasible for the industrial robots with a limited battery life.

In this work, we study two types of positioning algorithms in order to deal with the location uncertainty of the ANs without increasing the computational complexity. Firstly, we extend the 2D positioning method from [8] into a 3D geometry-based positioning method, named as the weighted centroid geometric (WCG). In the WCG, the location of a robot is estimated by fusing both the time of arrival (ToA) and the angle of arrival (AoA) measurements into the robot positioning algorithms. Secondly, instead of incorporating the location of both the robot and the ANs into the state vector of an EKF algorithm, we derive and formulate the EKF-based positioning algorithm with the location uncertainty of the ANs being mapped to the measurement noise statistics. Besides the 3D positioning accuracy, the vertical accuracy is also employed as a performance metric [7], as the vertical accuracy can be particularly crucial in certain applications that relies on robot-positioning in an indoor environment.

The remaining of this paper is organized as follows. First, the system model is described in Section II where the utilized path-loss model, observation models of the considered measurements as well as the location uncertainty model of the ANs are given separately. Both the geometry-based and the EKF-based positioning algorithms are described and formulated in Section III and IV, respectively. In Section V, the test scenario as well as the simulation-based results are present and examined. The conclusion and future works are summarized in the end.

II. System model

We consider a single-input-multiple-outputs (SIMO) positioning system for robot-based industrial applications where a flying robot transmits uplink (UL) pilot signals to the network edge (ANs) where the location-dependent measurements are acquired. In particular, the transmitted data is assumed to employ the form of an orthogonal frequency division multiplex (OFDM) signal sent periodically from the robot equipped with an omnidirectional antenna, while moving along a pre-designed trajectory. We also assume that the ANs are equipped with uniform rectangular antenna (URA) arrays and support

3D beamforming technique. The network edge estimates and collects ToA and AoA measurements and uploads them to a central unit, where the robot's location is then estimated. In this work, positioning is carried out at the network side in order to keep the computational burden on the robot to a minimum.

A. Path loss model and beamforming gains

The robot's location is denoted as $\mathbf{P}[i] = [x[i], y[i], z[i]]^T$ at the ith time-instant along the trajectory. Furthermore, we assume that there are $M[i]$ line-of-sight (LoS)-ANs at the considered time instant (for the sake of clarity we omit the time index of M for the rest of this paper). Based on the location geometry, the received signal strength (RSS) $P_{R,m}[i]$ in dBm at the ith time-instant from the robot to the mth LoS-AN located at $\mathbf{P}_{\text{AN},m} = [x_m, y_m, z_m]^T$ is written as

$$P_{R,m}[i] = P_T - \text{PL}\left(d_m[i]\right) + S\left(\mathbf{P}[i]\right) + G_T + G_R, \quad (1)$$

where P_T is the transmitted UL signal power in dBm, $\text{PL}\left(d_m[i]\right)$ in dB is the path-loss as a function of the Euclidean distance between the robot and the mth LoS-AN, denoted as $d_m[i] = \|\mathbf{P}[i] - \mathbf{P}_{\text{AN},m}\|$. Meanwhile, $S\left(\mathbf{P}[i]\right)$ represents the shadowing that depends on the robot's location. In this paper, we adopted the 3GPP indoor hotspot (InH) path-loss model with LoS path and a Gaussian distributed shadow fading [9]. Moreover, the beamforming gains at the transmitter and receiver are denoted as G_T and G_R, respectively where G_T is normalized to 0 dBi since the robot is equipped with an omnidirectional antenna, whereas G_R depends on the AoA since beamforming technique is enabled at all ANs. In this work, we assume that the G_R is obtained by an exhaustive 3D beam-training strategy in order to ensure that the UL pilot signals are received within the half-power beamwidth of the antenna at each LoS-AN. Note that the RSS values in (1) are not utilized for positioning as such, but rather applied to quantify the accuracy of both ToA and AoA measurements.

B. Observation model of location-dependent parameters

1) ToA measurements and clock offset model: The ToA observation model reflecting the distances between the LoS-ANs and the robot is expressed as

$$\hat{\boldsymbol{\tau}}[i] = \boldsymbol{b}[i] + \boldsymbol{f}_\tau\left(\mathbf{P}[i]\right) + \boldsymbol{n}_\tau[i], \quad (2)$$

where $\boldsymbol{b}[i] \in \mathbb{R}^{M\times 1}$ refers to the clock offset vector. Here, we model the clock offset as a Gaussian random process [10] that meets the synchronization requirement of 5G network, that is, $\boldsymbol{b}[i] \sim \mathcal{N}\left(\mathbf{0}_M, \boldsymbol{R}_{\text{clk}}\right)$ where $\boldsymbol{R}_{\text{clk}} = \sigma^2_{\text{clk}}\mathbf{I}_{M\times M}$ in which $\mathbf{0}_M$ and $\mathbf{I}_{M\times M}$ are vector containing M zeros and $M \times M$ identity matrix, respectively, and σ_{clk} is set to 10 ns [11]. The ToA observation function $\boldsymbol{f}_\tau\left(\mathbf{P}[i]\right)$ is then expressed as

$$\begin{aligned}\boldsymbol{f}_\tau\left(\mathbf{P}[i]\right) &= [\tau_1[i], \cdots, \tau_M[i]]^T \\ &= \left[\|\mathbf{P}[i] - \mathbf{P}_{\text{AN},1}\|, \cdots, \|\mathbf{P}[i] - \mathbf{P}_{\text{AN},M}\|\right]^T / c,\end{aligned} \quad (3)$$

where c is the speed of light. Furthermore, the variable $\boldsymbol{n}_\tau$ represents an additive Gaussian noise vector with zero-mean under the LoS scenario and non-zero mean under the non-ideal propagation conditions, such as non-line-of-sight (NLoS) propagation. Since the LoS scenario is typical in the future 5G ultra dense networks [12], the noise vector $\boldsymbol{n}_\tau[i]$ is modelled as a zero-mean Gaussian variable, that is, $\mathcal{N}\left(\mathbf{0}_M, \boldsymbol{R}_\tau[i]\right)$ with a diagonal noise covariance matrix $\boldsymbol{R}_\tau[i] = \text{diag}\left(\sigma^2_{\tau,1}, \cdots, \sigma^2_{\tau,M}\right)$. The noise variance of the mth ToA measurement, $\sigma^2_{\tau,m}$ (the time index omitted), is bounded by the following Cramér-Rao lower bound (CRLB) for OFDM signals [5, Ch.3]

$$\sigma^2_{\tau,m} \geq \frac{3P_n}{8\pi^2 f^2_{\text{sc}} P_{r,m}[i] M_u(M_u+1)(2M_u+1)}, \quad (4)$$

where f_{sc} represents the sub-carrier spacing, and $M_u = \frac{N_u-1}{2}$, N_u is the overall number of sub-carriers. Furthermore, $P_{r,m}[i]$ is the linear scale of RSS at the ith time instant of the mth AN calculated from (1) and P_n is the noise power over the entire bandwidth. It is worth noting that (4) applies only for OFDM with *uniformly distributed* energy among all the sub-carriers.

2) AoA measurements: The AoA measurements can also be utilized to estimate the direction of the robot's location based on the LoS propagation between every AN-robot pair [5]. In the considered 3D scenario, AoA observations consists of the elevation AoA as well as the azimuth AoA. Taking the URA's orientation into account, the AoA observation is expressed as

$$\hat{\boldsymbol{\phi}}[i] = \boldsymbol{f}_\phi\left(\mathbf{P}[i]\right) + \boldsymbol{\alpha} + \boldsymbol{n}_\phi[i], \quad (5)$$

where $\hat{\boldsymbol{\phi}}[i] \in \mathbb{R}^{2M\times 1}$ consists of the elevation AoA measurements $\hat{\boldsymbol{\varphi}}[i] \in \mathbb{R}^{M\times 1}$ as well as the azimuth AoA measurements $\hat{\boldsymbol{\theta}}[i] \in \mathbb{R}^{M\times 1}$. Furthermore, we denote the known angular offset due to the specific array orientations as $\boldsymbol{\alpha} \in \mathbb{R}^{2M\times 1}$, where $\boldsymbol{\alpha}$ contains the angular offsets along both elevation domain and azimuth domain denoted as $\boldsymbol{\alpha}_\varphi \in \mathbb{R}^{M\times 1}$ and $\boldsymbol{\alpha}_\theta \in \mathbb{R}^{M\times 1}$, respectively. Moreover, the AoA noise vector is also a zero-mean Gaussian process, that is, $\boldsymbol{n}_\phi[i] \sim \mathcal{N}\left(\mathbf{0}_M, \boldsymbol{R}_\phi[i]\right)$ with a noise covariance matrix $\boldsymbol{R}_\phi[i] = \text{diag}\left(\sigma^2_{\varphi,1}, \cdots, \sigma^2_{\varphi,M}, \sigma^2_{\theta,1}, \cdots, \sigma^2_{\theta,M}\right)$ (Same as with $\sigma^2_{\tau,m}$, we drop the time index here). The non-linear AoA observation function $\boldsymbol{f}_\phi\left(\cdot\right)$ in (5) consists of the observation function for elevation angle, denoted as $\boldsymbol{f}_\varphi\left(\cdot\right)$, and the observation function for azimuth angle, denoted as $\boldsymbol{f}_\theta\left(\cdot\right)$. Altogether, the AoA observation function w.r.t. $\mathbf{P}[i]$ is expressed as $\boldsymbol{f}_\phi\left(\mathbf{P}[i]\right) = \left[\boldsymbol{f}^T_\varphi\left(\mathbf{P}[i]\right), \boldsymbol{f}^T_\theta\left(\mathbf{P}[i]\right)\right]^T$, where

$$\boldsymbol{f}_\varphi\left(\mathbf{P}[i]\right) = \begin{bmatrix} \arcsin\left(\Delta z_1[i]/d_1[i]\right) \\ \vdots \\ \arcsin\left(\Delta z_M[i]/d_M[i]\right) \end{bmatrix}, \quad (6)$$

$$\boldsymbol{f}_\theta\left(\mathbf{P}[i]\right) = \begin{bmatrix} \text{atan}_2\left(\Delta y_1[i], \Delta x_1[i]\right) \\ \vdots \\ \text{atan}_2\left(\Delta y_M[i], \Delta x_M[i]\right) \end{bmatrix}, \quad (7)$$

in which $\Delta x_m[i] = x[i] - x_m$, $\Delta y_m[i] = y[i] - y_m$, and $\Delta z_m[i] = z[i] - z_m$ for all $m = 1, \ldots, M$. Additionally, arcsin and atan_2 denote the inverse sine function and four-quadrant inverse tangent function, respectively.

Assuming that the distance between any two adjacent antenna elements is half of the carrier wavelength c/f_c, and taking the azimuth AoA between the mth LoS-AN and the robot, i.e., θ_m as an example, the measurement noise variance of the mth azimuth AoA measurement, $\sigma^2_{\theta,m}$, is bounded by the CRLB that is derived based on [5, Ch.3] as

$$\sigma^2_{\theta,m} \geq \frac{6P_n}{L\left(L^2-1\right)P_{r,m}[i]\left(\pi\cos\theta_m\right)^2}, \tag{8}$$

where L is the number of antenna elements along the azimuth plane and $P_{r,m}[i]$ and P_n are the same variables as in (4). It is noteworthy that the angular CRLB depends on the geometry between the robot and the AN, because (8) reaches to infinity whenever the azimuth AoA approaches $\pm\pi/2$, and it suggests that for $\theta_m \to \pm\pi/2$, the effective aperture of the array grows smaller which results in the diminishing angular resolution of the array.

Additionally, since an $L \times L$ URA is utilized, we assume the angular resolution in both elevation and azimuth direction are the same, and hence, the noise statistics of the elevation AoA measurement, $\sigma^2_{\varphi,m}$, shares the same expression as (8). In (8), the given noise variance is analysed based on dividing the URA model into two separate uniform linear antenna (ULA) arrays including both azimuth and elevation angles. Thus, when appropriately utilizing measurements jointly from all URA antenna elements, the given AoA measurement noise variance can be even further reduced.

C. Location uncertainty of ANs

We denote the error-bearing locations of ANs as $\tilde{\mathbf{P}}_{\text{AN}} \in \mathbb{R}^{3\times M}$ that are known at the central unit whereas the actual ANs' locations are denoted as $\mathbf{P}_{\text{AN}} \in \mathbb{R}^{3\times M}$. Their relationship is expressed as

$$\tilde{\mathbf{P}}_{\text{AN}} = \mathbf{P}_{\text{AN}} + \boldsymbol{e}_{\text{AN}}, \tag{9}$$

where the uncertainty of ANs' locations is denoted as $\boldsymbol{e}_{\text{AN}} = [\boldsymbol{e}_{\text{AN},1}, \cdots, \boldsymbol{e}_{\text{AN},M}]$, in which $\boldsymbol{e}_{\text{AN},m}$ is defined as

$$\boldsymbol{e}_{\text{AN},m} \sim \mathcal{N}\left(\mathbf{0}_3, \text{diag}\left(\sigma^2_{\text{AN}}, \sigma^2_{\text{AN}}, \frac{\sigma^2_{\text{AN}}}{\beta^2}\right)\right). \tag{10}$$

In particular, since the horizontal plane in general occupies a much larger size than that of the vertical plane, we assume that the ANs' locations uncertainty in the z-direction is β times smaller than the uncertainty in x-direction (we use $\beta = 10$ in our simulations), while both x- and y- directions share the same uncertainty σ_{AN}. Note that σ^2_{AN} is not indexed as in this paper we assume that all the ANs suffer from the same level of location uncertainty. In order to obtain the statistics for the ANs' locations, e.g., a training database containing fingerprints can be employed. However, due to several error sources in estimating ANs' locations, the value of σ_{AN} is varied in the simulations to characterize different levels of such uncertainty.

III. Weighted Centroid Geometric Positioning

As the main contribution of this work, we now derive the proposed WCG approach based on the fusion of information from ToA and AoA measurements and the geometry relation between the LoS-AN and the robot as shown in Fig. 1. Throughout this section, *the time index is omitted for the sake of clarity*. With a perfect knowledge on the mth LoS-AN where $m = 1, \ldots, M$ and the corresponding noise-free ToA/AoA measurements, the robot location $\mathbf{P}$ can be acquired as

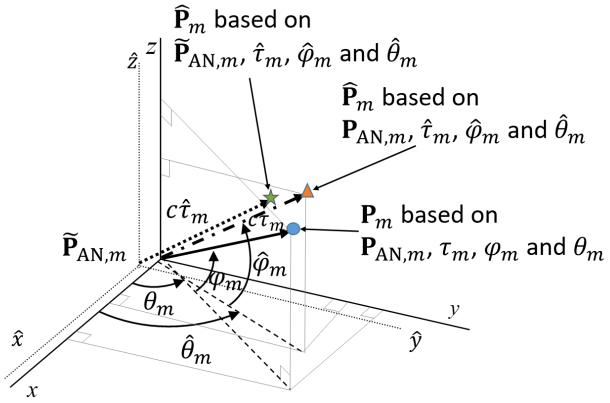

Fig. 1: 3D Geometry between the mth pair of LoS-AN-robot in the presence of measurements and AN location uncertainty.

$$\mathbf{P} = \begin{bmatrix} x \\ y \\ z \end{bmatrix} = \begin{bmatrix} x_m + c\tau_m \cos\varphi_m \cos\theta_m \\ y_m + c\tau_m \cos\varphi_m \sin\theta_m \\ z_m + c\tau_m \sin\varphi_m \end{bmatrix}. \tag{11}$$

However, in practical scenarios, especially in the industrial environments, not only the measurements are corrupted by noise, but also there might be errors in the assumed ANs' locations. By taking into account both measurement noise and the location uncertainty of the ANs, (11) is expressed as

$$\hat{\mathbf{P}}_m = \begin{bmatrix} \hat{x}_m \\ \hat{y}_m \\ \hat{z}_m \end{bmatrix} = \begin{bmatrix} \tilde{x}_m + c\hat{\tau}_m \cos\hat{\varphi}_m \cos\hat{\theta}_m \\ \tilde{y}_m + c\hat{\tau}_m \cos\hat{\varphi}_m \sin\hat{\theta}_m \\ \tilde{z}_m + c\hat{\tau}_m \sin\hat{\varphi}_m \end{bmatrix}, \tag{12}$$

where the location of the mth LoS-AN known to the central unit is denoted as $\tilde{\mathbf{P}}_{\text{AN},m} = [\tilde{x}_m, \tilde{y}_m, \tilde{z}_m]^T$. The (green) star marker in Fig. 1, that is acquired by applying (12), is the position estimate based on imperfect AN location knowledge as well as the noisy measurements between the mth pair of LoS-AN and robot. Therefore, we obtain in total M position estimates from overall M pairs of LoS-ANs and robot, denoted in a matrix form as $\hat{\mathbf{P}} = \left[\hat{\mathbf{P}}_1, \cdots, \hat{\mathbf{P}}_M\right]$. In order to combine the obtained M position estimates into a single robot position estimate, a weight vector is designed by considering the quality of measurements and available clock statistics, such that

$$\begin{aligned} \boldsymbol{w} &= [w_1, \cdots, w_M]^T \\ &= \left[\left(\sigma^2_{\tau,1} + \sigma^2_{\text{clk}}\right)^{-1}, \cdots, \left(\sigma^2_{\tau,M} + \sigma^2_{\text{clk}}\right)^{-1}\right]^T. \end{aligned} \tag{13}$$

Finally, the position estimate obtained by the WCG is the product of the estimate AN location matrix $\hat{\mathbf{P}}$ and the normalized weight vector $\tilde{\boldsymbol{w}}$ such that

$$\hat{\mathbf{P}}_{\text{WCG}} = \hat{\mathbf{P}}\tilde{\boldsymbol{w}}, \tag{14}$$

where $\tilde{\boldsymbol{w}} = \boldsymbol{w}/\sum_{m=1}^{M} w_m$.

IV. Extended Kalman filter based positioning

As a comparison method for the proposed WCG positioning method that only relies on the available measurements at the current state and no prior information is needed, we present a well-known tracking algorithm for robot positioning that is, an EKF. Several works such as [6], [7], [13] have presented the positioning performance achieved by the EKF under 5G mobile networks. Given the available measurements, we consider two EKF-based methods, one utilizes both ToA and AoA measurements, denoted as 'EKF T+A', while the other utilizes only AoA measurements, denoted as 'EKF A'. By considering the location, velocity and acceleration of the robot, the state vector at the ith time instant is given as

$$\mathbf{s}[i] = [x[i], y[i], z[i], v_x[i], v_y[i], v_z[i], a_x[i], a_y[i], a_z[i]]^T, \tag{15}$$

where $x[i], y[i], z[i]$ refers to the location of the robot in x-, y- and z-coordinate, and $v_x[i], v_y[i], v_z[i]$ are the velocity components in terms of x-axis, y-axis and z-axis. Similarly, we have the acceleration components in all three directions, denoted as $a_x[i], a_y[i], a_z[i]$. Furthermore, we assume that the state transition between any two adjacent states follows a linear model and the observation model that connects the state vector with the measurements obeys a non-linear model, which are described in a general form as [14]

$$\begin{aligned} \mathbf{s}[i] &= \mathbf{F}\mathbf{s}[i-1] + \mathbf{v}[i] \\ \mathbf{y}[i] &= \mathbf{h}\left(\mathbf{s}[i]\right) + \mathbf{w}[i], \end{aligned} \tag{16}$$

where $\mathbf{F}$ and $\mathbf{h}$ are the linear state transition matrix and non-linear observation function, respectively, $\mathbf{v}[i] \sim \mathcal{N}(0, \mathbf{Q})$ is the state process noise vector, and $\mathbf{w}[i] \sim \mathcal{N}(0, \mathbf{R})$ refers to as the measurement noise vector. Throughout this paper, we denote $\mathbf{y}[i]$ as the measurement vector that contains the available measurements at the ith time step. Assuming the models in (16) and the statistics of the initial state, the predicted state $\hat{\mathbf{s}}^-[i]$ and state covariance matrix $\hat{\mathbf{\Sigma}}^-[i]$ can be evaluated as

$$\begin{aligned} \hat{\mathbf{s}}^-[i] &= \mathbf{F}\hat{\mathbf{s}}[i-1] \\ \hat{\mathbf{\Sigma}}^-[i] &= \mathbf{F}\hat{\mathbf{\Sigma}}[i-1]\mathbf{F}^T + \mathbf{Q}. \end{aligned} \tag{17}$$

Both a priori mean and covariance estimates in (17) are to be corrected by incorporating the incoming measurements at the specific time instant using the following steps

$$\begin{aligned} \mathbf{K}[i] &= \hat{\mathbf{\Sigma}}^-[i]\mathbf{H}^T[i]\left(\mathbf{H}[i]\hat{\mathbf{\Sigma}}^-[i]\mathbf{H}^T[i] + \mathbf{R}\right)^{-1} \\ \hat{\mathbf{s}}[i] &= \hat{\mathbf{s}}^-[i] + \mathbf{K}[i]\left(\mathbf{y}[i] - \mathbf{h}\left(\hat{\mathbf{s}}^-[i]\right)\right) \\ \hat{\mathbf{\Sigma}}[i] &= \left(\mathbf{I} - \mathbf{K}[i]\mathbf{H}[i]\right)\hat{\mathbf{\Sigma}}^-[i], \end{aligned} \tag{18}$$

where $\hat{\mathbf{s}}[i]$ and $\hat{\mathbf{\Sigma}}[i]$ are the a posteriori estimate of the state vector and state covariance matrix, respectively. In addition, the state-dependent Kalman gain matrix is denoted as $\mathbf{K}[i]$, and $\mathbf{H}[i]$ refers to the Jacobian matrix of the observation function $\mathbf{h}(\cdot)$ evaluated at the predicted state $\hat{\mathbf{s}}^-[i]$.

Since an indoor industrial environment is under consideration, the robot is assumed to move with a constant acceleration which indicates that the acceleration remains almost constant between consecutive states. Hence, the state transition matrix $\mathbf{F}$ and state noise covariance matrix $\mathbf{Q}$ can be described as [6], [15]

$$\begin{aligned} \mathbf{F} &= \begin{bmatrix} \mathbf{I}_{3\times3} & \Delta t\mathbf{I}_{3\times3} & \frac{\Delta t^2}{2}\mathbf{I}_{3\times3} \\ \mathbf{0}_{3\times3} & \mathbf{I}_{3\times3} & \Delta t\mathbf{I}_{3\times3} \\ \mathbf{0}_{3\times3} & \mathbf{0}_{3\times3} & \mathbf{I}_{3\times3} \end{bmatrix} \\ \mathbf{Q} &= \begin{bmatrix} \frac{\Delta t^5\mathbf{I}_{3\times3}}{20} & \frac{\Delta t^4\mathbf{I}_{3\times3}}{8} & \frac{\Delta t^3\mathbf{I}_{3\times3}}{6} \\ \frac{\Delta t^4\mathbf{I}_{3\times3}}{8} & \frac{\Delta t^3\mathbf{I}_{3\times3}}{3} & \frac{\Delta t^2\mathbf{I}_{3\times3}}{2} \\ \frac{\Delta t^3\mathbf{I}_{3\times3}}{6} & \frac{\Delta t^2\mathbf{I}_{3\times3}}{2} & \Delta t\mathbf{I}_{3\times3} \end{bmatrix} \sigma_q^2, \end{aligned} \tag{19}$$

where Δt represents the time-interval between two adjacent states, and σ_q^2 denotes the uncertainty in the acceleration, that is, the variance of the acceleration noise. The 3×3 identity matrix is denoted as $\mathbf{I}_{3\times3}$. In terms of tuning the process noise covariance matrix $\mathbf{Q}$ for both EKFs, σ_q^2 has been adjusted such that a centimeter-level 3D RMSE is achieved when $\sigma_{\text{AN}} = 0$. Thereafter, the same $\mathbf{Q}$ matrix has been applied for $\sigma_{\text{AN}} > 0$.

When both ToA and AoA measurements are considered for positioning, the measurement vector $\mathbf{y}_{\text{T+A}}[i] \in \mathbb{R}^{3M+1}$ is essentially the fusion of (2) and (5) which is written as $\mathbf{y}_{\text{T+A}}[i] = \left[\hat{\boldsymbol{\tau}}^T[i], \hat{\boldsymbol{\phi}}^T[i]\right]^T$. Similarly, the observation function of the EKF T+A can be stacked as $\mathbf{h}_{\text{T+A}}(\mathbf{s}^-[i]) = \left[\boldsymbol{f}_\tau^T, \boldsymbol{f}_\phi^T\right]^T$. Moreover, the Jacobian matrix of $\mathbf{h}_{\text{T+A}}(\mathbf{s}^-[i])$ is denoted as $\mathbf{H}_{\text{T+A}}[i] \in \mathbb{R}^{3M\times9}$ and it is given as $\mathbf{H}_{\text{T+A}}[i] = \left[\mathbf{H}_\tau^T[i], \mathbf{H}_\phi^T[i]\right]^T$, in which $\mathbf{H}_\tau^T[i]$ and $\mathbf{H}_\phi^T[i]$ denote the Jacobian matrix of the ToA measurements and AoA measurements as

$$\mathbf{H}_\tau[i] = \begin{bmatrix} \frac{\Delta\hat{x}_1[i]}{c\hat{d}_1[i]} & \frac{\Delta\hat{y}_1[i]}{c\hat{d}_1[i]} & \frac{\Delta\hat{z}_1[i]}{c\hat{d}_1[i]} & \mathbf{0}_{1\times6} \\ \vdots & \vdots & \vdots & \vdots \\ \frac{\Delta\hat{x}_M[i]}{c\hat{d}_M[i]} & \frac{\Delta\hat{y}_M[i]}{c\hat{d}_M[i]} & \frac{\Delta\hat{z}_M[i]}{c\hat{d}_M[i]} & \mathbf{0}_{1\times6} \end{bmatrix}, \tag{20}$$

$$\mathbf{H}_\phi[i] = \begin{bmatrix} -\frac{\Delta\hat{x}_1[i]\Delta\hat{z}_1[i]}{\hat{d}_1^2[i]\hat{d}_{\text{2D},1}[i]} & -\frac{\Delta\hat{y}_1[i]\Delta\hat{z}_1[i]}{\hat{d}_1^2[i]\hat{d}_{\text{2D},1}[i]} & \frac{\hat{d}_{\text{2D},1}[i]}{\hat{d}_1^2[i]} & \mathbf{0}_{1\times6} \\ \vdots & \vdots & \vdots & \vdots \\ -\frac{\Delta\hat{x}_M[i]\Delta\hat{z}_M[i]}{\hat{d}_M^2[i]\hat{d}_{\text{2D},M}[i]} & -\frac{\Delta\hat{y}_M[i]\Delta\hat{z}_M[i]}{\hat{d}_M^2[i]\hat{d}_{\text{2D,M}}[i]} & \frac{\hat{d}_{\text{2D},M}[i]}{\hat{d}_M^2[i]} & \mathbf{0}_{1\times6} \\ -\frac{\Delta\hat{y}_1[i]}{\hat{d}_{\text{2D},1}[i]} & \frac{\Delta\hat{x}_1[i]}{\hat{d}_{\text{2D},1}[i]} & 0 & \mathbf{0}_{1\times6} \\ \vdots & \vdots & \vdots & \vdots \\ -\frac{\Delta\hat{y}_M[i]}{\hat{d}_{\text{2D},M}[i]} & \frac{\Delta\hat{x}_M[i]}{\hat{d}_{\text{2D},M}[i]} & 0 & \mathbf{0}_{1\times6} \end{bmatrix}, \tag{21}$$

where $\Delta\hat{x}_m[i] = \hat{x}[i] - \tilde{x}_m$, $\Delta\hat{y}_m[i] = \hat{y}[i] - \tilde{y}_m$, $\Delta\hat{z}_m[i] = \hat{z}[i] - \tilde{z}_m$, $\hat{d}_m[i] = \sqrt{\Delta\hat{x}_m^2[i] + \Delta\hat{y}_m^2[i] + \Delta\hat{z}_m^2[i]}$ and the 2D distance between the predicted robot's location and the mth AN is denoted as $\hat{d}_{\text{2D},m}[i] = \sqrt{\Delta\hat{x}_m^2[i] + \Delta\hat{y}_m^2[i]}$, where $m = 1, \ldots, M$.

In general, without the uncertainty of ANs' location, the measurement noise covariance matrix is denoted as $\boldsymbol{R}_{\text{T+A}}[i] = \text{blkdiag}\{\boldsymbol{R}_\tau[i], \boldsymbol{R}_\phi[i]\}$ for EKF T+A, and $\boldsymbol{R}_{\text{A}}[i] = \boldsymbol{R}_\phi[i]$ for EKF A. However, in the considered scenario and application, the error statistics that incurred due to the assumed ANs'

location uncertainty and clock bias have to be incorporated in the observation model and reflected by the measurement noise covariance matrix. That being said, the uncertainty in the location of the ANs must be mapped to the measurement noise statistics. A linearization is therefore implemented for each AN-robot pair in order to perform the nonlinear mapping from multi-dimension AN location error to a single dimension measurement error. Hence, the resulting $\boldsymbol{R}_{\text{T+A}}[i]$ is given as

$$\boldsymbol{R}_{\text{T+A}}[i] = \text{blkdiag}\left\{\boldsymbol{R}_{\tau}[i] + \tilde{\boldsymbol{R}}_{\tau}[i] + \boldsymbol{R}_{\text{clk}}, \boldsymbol{R}_{\phi}[i] + \tilde{\boldsymbol{R}}_{\phi}[i]\right\}, \tag{22}$$

where $\tilde{\boldsymbol{R}}_{\tau}[i] \in \mathbb{R}^{M\times M}$ and $\tilde{\boldsymbol{R}}_{\phi}[i] \in \mathbb{R}^{2M\times 2M}$. The $\tilde{}$-sign is used to represent the extra noise statistics to ToA and AoA measurements caused by the location uncertainty of ANs.

Since all the ANs are assumed to suffer from the same location uncertainty as discussed in II-C, we express $\tilde{\boldsymbol{R}}_{\tau}[i]$ and $\tilde{\boldsymbol{R}}_{\phi}[i]$ as

$$\tilde{\boldsymbol{R}}_{\tau}[i] = \left[\frac{\partial \boldsymbol{f}_{\tau}}{\partial \tilde{\mathbf{P}}_{\text{AN}}}\bigg|_{\hat{\mathbf{s}}^{-}[i]}\right] \boldsymbol{R}_{\text{AN}} \left[\frac{\partial \boldsymbol{f}_{\tau}}{\partial \tilde{\mathbf{P}}_{\text{AN}}}\bigg|_{\hat{\mathbf{s}}^{-}[i]}\right]^{T} \tag{23}$$

$$\tilde{\boldsymbol{R}}_{\phi}[i] = \left[\frac{\partial \boldsymbol{f}_{\phi}}{\partial \tilde{\mathbf{P}}_{\text{AN}}}\bigg|_{\hat{\mathbf{s}}^{-}[i]}\right] \boldsymbol{R}_{\text{AN}} \left[\frac{\partial \boldsymbol{f}_{\phi}}{\partial \tilde{\mathbf{P}}_{\text{AN}}}\bigg|_{\hat{\mathbf{s}}^{-}[i]}\right]^{T}, \tag{24}$$

where $\boldsymbol{R}_{\text{AN}} = \text{diag}\left(\sigma^2_{\text{AN}}, \sigma^2_{\text{AN}}, \frac{\sigma^2_{\text{AN}}}{\beta^2}\right)$ denotes the covariance matrix of ANs' location uncertainty defined in (10). Moreover, the Jacobian matrix w.r.t. the ANs can be obtained by simply taking the opposite sign of the non-zero terms in (20) and (21) yielding

$$\frac{\partial \boldsymbol{f}_{\tau}}{\partial \tilde{\mathbf{P}}_{\text{AN}}}\bigg|_{\hat{\mathbf{s}}^{-}[i]} = \begin{bmatrix} \frac{-\Delta\hat{x}_1[i]}{c\hat{d}_1[i]} & \frac{-\Delta\hat{y}_1[i]}{c\hat{d}_1[i]} & \frac{-\Delta\hat{z}_1[i]}{c\hat{d}_1[i]} \\ \vdots & \vdots & \vdots \\ \frac{-\Delta\hat{x}_M[i]}{c\hat{d}_M[i]} & \frac{-\Delta\hat{y}_M[i]}{c\hat{d}_M[i]} & \frac{-\Delta\hat{z}_M[i]}{c\hat{d}_M[i]} \end{bmatrix} \tag{25}$$

$$\frac{\partial \boldsymbol{f}_{\phi}}{\partial \tilde{\mathbf{P}}_{\text{AN}}}\bigg|_{\hat{\mathbf{s}}^{-}[i]} = \begin{bmatrix} \frac{\Delta\hat{x}_1[i]\Delta\hat{z}_1[i]}{\hat{d}^2_1[i]\hat{d}_{\text{2D},1}[i]} & \frac{\Delta\hat{y}_1[i]\Delta\hat{z}_1[i]}{\hat{d}^2_1[i]\hat{d}_{\text{2D},1}[i]} & -\frac{\hat{d}_{\text{2D},1}[i]}{\hat{d}^2_1[i]} \\ \vdots & \vdots & \vdots \\ \frac{\Delta\hat{x}_M[i]\Delta\hat{z}_M[i]}{\hat{d}^2_M[i]\hat{d}_{\text{2D},M}[i]} & \frac{\Delta\hat{y}_M[i]\Delta\hat{z}_M[i]}{\hat{d}^2_M[i]\hat{d}_{\text{2D,M}}[i]} & -\frac{\hat{d}_{\text{2D},M}[i]}{\hat{d}^2_M[i]} \\ \frac{\Delta\hat{y}_1[i]}{\hat{d}_{\text{2D},1}[i]} & -\frac{\Delta\hat{x}_1[i]}{\hat{d}_{\text{2D},1}[i]} & 0 \\ \vdots & \vdots & \vdots \\ \frac{\Delta\hat{y}_M[i]}{\hat{d}_{\text{2D},M}[i]} & -\frac{\Delta\hat{x}_M[i]}{\hat{d}_{\text{2D},M}[i]} & 0 \end{bmatrix}, \tag{26}$$

where $\Delta\hat{x}_m[i]$, $\Delta\hat{y}_m[i]$, $\Delta\hat{z}_m[i]$, $\hat{d}_m[i]$ and $\hat{d}_{\text{2D},m}[i]$ for $m = 1,\ldots,M$ refer to the same notations as (21).

V. Test scenario and simulation-based results

A. Scenario deployment

The positioning performance of the studied positioning algorithms (i.e., WCG, EKF A and EKF T+A) is tested with a realistic wall-divided indoor map with a length of 150 m, width of 112 m, and height of 4 m as shown in the left plot of Fig. 2. The overall trajectory is plotted in the blue curve along which the robot is moving at nearly constant velocities, around 1.1 m/s (human walking speed is around 0.6 m/s), and at a linearly varying height between 1 m and 2 m given in the right plot of Fig. 2. In particular, the corners of the trajectory are smoothed in order to reflect a practical trajectory of a moving robot. Moreover, we design the ANs to be installed on the walls at 3m height shown in red circle markers, and the corresponding array orientations of the ANs, i.e., the angular offsets $\boldsymbol{\alpha}$ are assumed to be known. In particular, we set $\boldsymbol{\alpha}_{\varphi} = \mathbf{0}_M$, whereas the values of $\boldsymbol{\alpha}_{\theta}$, i.e., the orientations in the azimuth domain, are initialized so that the arrays are parallel to the corresponding wall. Furthermore, there are at least four LoS-ANs available along the studied trajectory, and the AN density is around 1.24/25m^2. Finally, we summarize the UL pilot signal parameters used in our simulations in Table I. Note that the carrier frequency is chosen at the millimetre wave (mmWave) band at 39 GHz with an approximate of 123 MHz signal bandwidth. In order to enhance the received signal strength at the ANs, the transmit power is set at 27 dBm which can be further reduced in a multi-robot scenario in order to ease the interference level.

TABLE I: Configuration of the UL OFDM pilot signal

Parameter	Value
Carrier frequency f_c	39 GHz
Sub-carrier spacing f_{sc}	120 kHz
No. of sub-carrier N_u	1024
Signal bandwidth B_w	123 MHz
Transmit power P_T	27 dBm
Receive beamforming gain G_R	20 dBi

B. Performance evaluation

The cumulative distribution function of the ToA measurement error as well as the AoA measurement error are shown in Fig. 3 where the values of the horizontal axis are described in meters for ToA measurement error, and in degrees for the AoA measurement error. Based on the results, it can be seen that the ToA errors are generally below $\pm$10m while the AoA errors rarely reaches beyond $\pm 0.5^{\circ}$. The behavior of the ToA measurement errors can be explained based on the ToA observation model (2) where the considered error sources consists of the thermal noise as well as the synchronization error with a 10ns standard deviation that corresponds to 3m error in distance. We point out here that the thermal noise error is dominated by the synchronization error as the former returns a ToA error in the magnitude of 0.1 - 8 cm owing to the wide signal bandwidth B_w. Compared to the ToA measurements, the AoA measurements seem to be more accurate as 95% of the errors for both the elevation and azimuth angle are within $\pm 0.5^{\circ}$. However, the small values in degrees does not necessarily indicate a better positioning accuracy since even a small error in the AoA measurements may lead to significant positioning errors when the distance between the robot and a given AN is large.

Both the 3D and vertical RMSE as a function of the location uncertainty of the ANs σ_{AN} (along the x-direction)

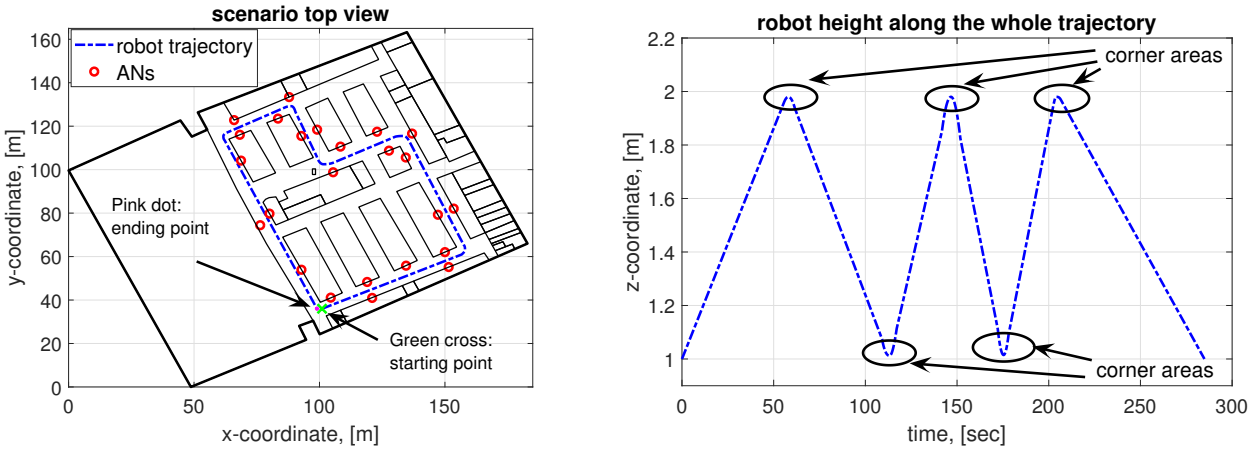

Fig. 2: Left plot: The top view of the deployed indoor scenario, where the walls are illustrated with a black color. The robot starts from the green cross and ends in the pink dot. Blue line represents the robot trajectory and red markers denote the locations of the ANs. Right plot: The robot trajectory in z-coordinate. To reflect a dynamic movement also in the vertical direction, a linear behavior is adopted.

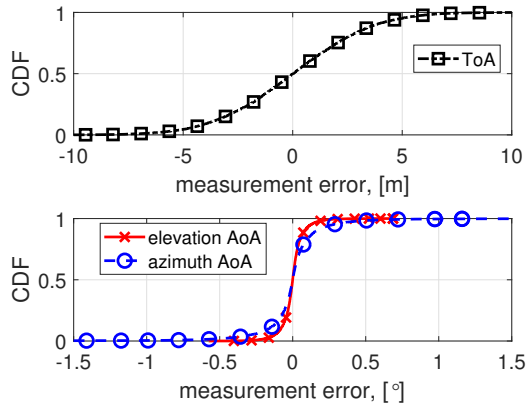

Fig. 3: The cumulative distribution function (CDF) of the ToA measurement error (in meters) and AoA measurement error (in degrees) that were utilized as the inputs of the considered positioning algorithms.

are given in Fig. 4. Note that the results is obtained based on 2000 simulation trials through the whole trajectory. The ANs' locations $\tilde{\mathbf{P}}_{\text{AN}}$, known at the central unit are initialized based on (9) in the beginning of each trial. Moreover, the location estimates of both considered EKFs are initialized around the reference location using the standard deviations of 1 m and 0.1 m in horizontal and vertical direction, respectively. Based on the obtained results, the EKF-based approaches outperform the WCG in terms of both 3D and vertical RMSE whenever the uncertainty in ANs' locations remains small enough i.e., $\sigma_{\text{AN}} \leq$ 0.5m, in which case, the EKFs are seen as better positioning solutions. On the other hand, the positioning performance of the EKFs degrades more severely than the WCG when σ_{AN} raises beyond 0.5m although a worse performance is seen to all the algorithms. One possible reason for the vast drop in terms of positioning performance of the EKFs especially at relative high σ_{AN} lies in the un-fulfillment of linearization of the nonlinear observation functions $\boldsymbol{f}_\tau$, $\boldsymbol{f}_\varphi$ and $\boldsymbol{f}_\theta$ w.r.t. the $\hat{\mathbf{s}}^-$ due to the highly un-precise location of the ANs contained in all the nonlinear observation functions. Numerically, the 3D/vertical RMSE of EKF T+A and EKF A raise to about 19m/5.2m and 29m/7.5m respectively whereas that of the WCG are kept roughly at 7m/0.6m at the highest considered uncertainty of ANs' locations, i.e., $\sigma_{\text{AN}} = 5$m. It has been observed that the WCG distinctly demonstrates a better robustness to higher location uncertainty of the ANs than the EKFs under the considered scenario and assumptions.

TABLE II: Computational complexity of positioning algorithms

Algorithm	Computational Complexity
EKFs	$\mathcal{O}(MN_s^2)$+$\mathcal{O}(M^2N_s)$
WCG	$\mathcal{O}(M)$

In addition to the positioning accuracy, we analyze and compare the computational complexity of all the algorithms in terms of the overall number of the involved real multiplications at *a single time instant*. According to [16], there are $21MN_s^2 + 144M^2N_s + 3MN_s$ and $14MN_s^2 + 64M^2N_s + 2MN_s$ real multiplications for EKF T+A and EKF A, respectively where M is denoted as the number of LoS-ANs and N_s refers to the number of entries in the state vector (15). Meanwhile, we computed that there are in total $11M$ real multiplications involved for WCG. Finally, the computational complexity in terms of $\mathcal{O}$ of EKFs and WCG are summarized in Table II.

VI. Conclusions and Future Work

In this paper, we developed and formulated two types of positioning algorithms with the location uncertainty of the ANs being considered and modelled statistically. The first method is a 3D geometry-based positioning approach utilizing both the ToA and AoA measurements. The second one is based on the Bayesian frame work, i.e., the EKF-based approach with the ANs' location uncertainty being mapped into the measurement error statistic. Additionally, the clock errors were

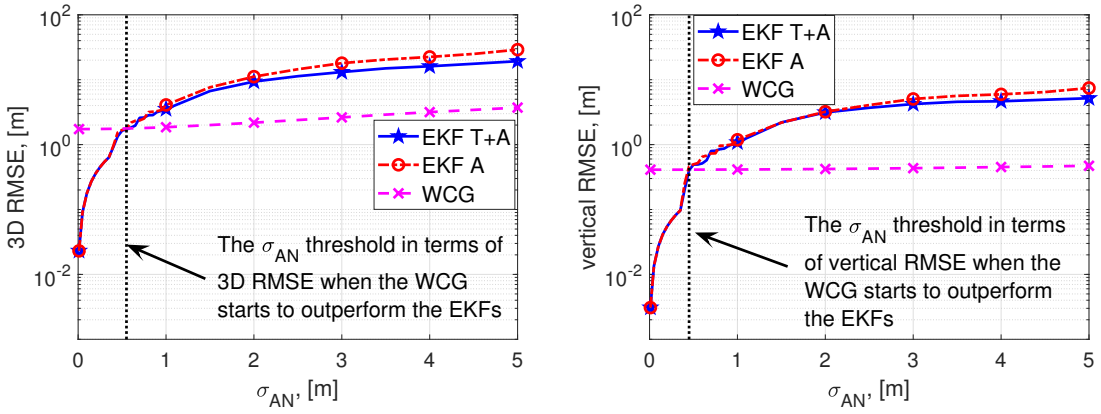

Fig. 4: Left plot: 3D RMSE of different positioning methods as a function of AN uncertainty σ_{AN}. Right plot: Vertical RMSE of different positioning methods as a function of AN uncertainty σ_{AN}.

also taken into consideration. The 3D and vertical RMSE as well as the number of operations needed to implement the considered algorithms (at one time instant) were utilized as the metrics for comparison. The numerical results showed that the utilized EKF-based algorithms remain as a better choice in terms of both 3D and vertical RMSE performances as long as the error contained in the location of ANs was kept at less than 0.5m (i.e., standard deviation along the x-direction). On the other hand, the proposed geometry-based approach, namely the WCG, was capable of maintaining a higher positioning accuracy than EKF-based approaches when exposed to the ANs locations uncertainty larger than 0.5m (standard deviation error), thus yielding a higher robustness. Nevertheless, we point out that the performance threshold (the σ_{AN} where RMSE curves of both EKFs and WCG cross) may vary for a different assumption/scenarios. The main advantage of the proposed WCG approach comes from the huge reduction in the computational complexity compared with considered EKFs, which makes it a very promising candidate for sensor and robot positioning in industrial environments where the ANs are not precisely known or located. Future work will concentrate on the simultaneously estimation of both the robots and ANs locations, as well as on mapping the uncontrolled environment through simultaneous localization and mapping (SLAM) algorithms.

Acknowledgements

The authors express their warm thanks to the Academy of Finland (project 313039) for its financial support on this work.

References

[1] 3GPP TR 22.872 V16.0.0 Technical Specification Group Services and System Aspects, "Study on positioning use cases (Release 16)," Jun 2018.

[2] J. Yin, Q. Wan, S. Yang, and K. C. Ho, "A simple and accurate tdoa-aoa localization method using two stations," *IEEE Signal Processing Letters*, vol. 23, no. 1, pp. 144–148, Jan 2016.

[3] H. Naseri and V. Koivunen, "A Bayesian algorithm for distributed network localization using distance and direction data," *IEEE Transactions on Wireless Communications*, Aug 2017.

[4] S. Tomic, M. Beko, R. Dinis, and P. Montezuma, "A Closed-Form Solution for RSS/AoA Target Localization by Spherical Coordinates Conversion," *IEEE Wireless Communications Letters*, vol. 5, no. 6, pp. 680–683, Dec 2016.

[5] S. Sand, A. Dammann, and C. Mensing, *Positioning in Wireless Communication Systems, John Wiley & Sons Ltd.*, Jun 2014.

[6] J. Talvitie, T. Levanen, M. Koivisto, K. Pajukoski, M. Renfors, and M. Valkama, "Positioning of high-speed trains using 5G new radio synchronization signals," in *2018 IEEE Wireless Communications and Networking Conference (WCNC)*, April 2018, pp. 1–6.

[7] M. Koivisto, M. Costa, A. Hakkarainen, K. Leppänen, and M. Valkama, "Joint 3D positioning and network synchronization in 5G ultra-dense networks using UKF and EKF," in *2016 IEEE Globecom Workshops (GC Wkshps)*, Dec 2016, pp. 1–7.

[8] M. W. Khan, N. Salman, A. H. Kemp, and L. Mihaylova, "Localisation of sensor nodes with hybrid measurements in wireless sensor networks," *Sensors*, vol. 16, no. 7, 2016. [Online]. Available: http://www.mdpi.com/1424-8220/16/7/1143

[9] 3GPP TR 38.900 V15.0.0 Technical Specification Group Radio Access Network, "Study on channel model for frequency spectrum above 6 GHz (Release 15)," Jun 2018.

[10] L. Moody, "Sensors, measurement fusion and missile trajectory optimisation," PhD thesis, Cranfield University, July 2003.

[11] H. Li, L. Han, R. Duan, and G. M. Garner, "Analysis of the synchronization requirements of 5G and corresponding solutions," *IEEE Communications Standards Magazine*, vol. 1, no. 1, pp. 52–58, March 2017.

[12] J. G. Andrews, S. Buzzi, W. Choi, S. V. Hanly, A. Lozano, A. C. K. Soong, and J. C. Zhang, "What will 5G be?" *IEEE Journal on Selected Areas in Communications*, vol. 32, no. 6, pp. 1065–1082, June 2014.

[13] E. Rastorgueva-Foi, M. Koivisto, M. Valkama, M. Costa, and K. Leppänen, "Localization and tracking in mmwave radio networks using beam-based DoD measurements," in *2018 8th International Conference on Localization and GNSS (ICL-GNSS)*, June 2018, pp. 1–6.

[14] D. Simon, *Optimal State Estimation: Kalman, H Infinity, and Nonlinear Approaches*. New York, NY, USA: Wiley-Interscience, 2006.

[15] M. Koivisto, J. Talvitie, M. Costa, K. Leppänen, and M. Valkama, "Joint cmwave-based multiuser positioning and network synchronization in dense 5G networks," in *2018 IEEE Wireless Communications and Networking Conference (WCNC)*, April 2018, pp. 1–6.

[16] S.-Y. Hou, S.-H. Chang, and H.-S. Hung, "Predictive Angle Tracking Algorithm Based on Extended Kalman Filter," in *Sensor Array*, W. Yang, Ed. IntechOpen, 2012. [Online]. Available: https://doi.org/10.5772/35507